ECCOMAS Congress 2016
VII European Congress on Computational Methods in Applied Sciences and Engineering
M. Papadrakakis, V. Papadopoulos, G. Stefanou, V. Plevris (eds.)
Crete Island, Greece, 5–10 June 2016

MODELING OF NON-SPHERICAL, ELONGATED PARTICLES FOR INDUSTRIAL SUSPENSION FLOW SIMULATION

Jakob D. Redlinger-Pohn[1], Lisa M. König[1], Christoph Kloss[2], Christoph Goniva[2], and Stefan Radl[1]

[1] Institute of Process and Particle Engineering, Graz University of Technology
Inffeldgasse 13/III, 8010 Graz, Austria
e-mail: redlinger-pohn@tugraz.at, lisa.koenig@tugraz.at, radl@tugraz.at

[2] DCS Computing GmbH
Industriezeile 35, 4020 Linz, Austria
e-mail: christoph.kloss@dcs-computing.com, christoph.goniva@dcs-computing.com

Keywords: Open-Source Code, Euler-Lagrange Simulation, Elongated Particles, Suspension Flow, Particle Segregation

Abstract. *Euler-Lagrange (EL) simulations of particulate suspension flow are an important tool to understand and predict multiphase flow in nature and industrial applications. Unfortunately, solid-liquid suspensions are often of (mathematically) stiff nature, i.e., the relaxation time of suspended particles may be small compared to relevant flow time scales. Involved particles are typically in the size range from µm to mm, and of non-spherical shape, e.g., elongated particles such as needle-shaped crystals and/or natural and man-made fibres. Depending on their aspect ratio and bending stiffness, those particles can be treated as rigid, or flexible. In this paper we present a recent implementation into the open-source LIGGGHTS® and CFDEM® software package for the simulation of systems involving stiff non-spherical, elongated particles. A newly implemented splitting technique of the coupling forces and torques, following the ideas of Fan and Ahmadi (J. Aerosol Sci. 26, 1995), allows significantly larger coupling intervals, leading to a substantial reduction in the computational cost. Hence, large-scale industrial systems can be simulated in an acceptable amount of time. We first present our modeling approach, followed by the verification of our code based on benchmark problems. Second, we present results of one-way coupled CFD-DEM simulations. Our simulations reveal segregation of fibres in dependence on their length due to fibre-fluid interaction in torus flow.*

1 INTRODUCTION

Understanding the transport of suspended particles is of great importance for the rational design of industrial equipment. Early studies concentrated on suspension of spherical particles due to their relative simplicity. However, such systems are rarely found in industrial application and rather limited to academic cases, i.e. spherical glass beads in suspensions. Thus the application of simulation results for the design of industrial equipment might not be advisable. In the last two decades, efforts were made to model and simulate elongated particles, i.e. cellulose fibres, needle shaped crystals, in suspension flow. We will review selection of recent studies in the following chapter. We then introduce our simulation approach which is based entirely on open-source code, i.e., OpenFOAM, LIGGGHTS®, and CFDEM®. The capabilities of our code will be demonstrated on hand of an examples of suspension flow of cellulose fibres.

1.1 Approaches to simulate Elongated Particles

Most of the previous studies [1] use an Euler-Lagrange approach to simulate the suspension flow of elongated particles. It allows the tracking of individual particle and thus to describe the segregation and orientation of single particles in suspension flow. For example, Soldati and Marchioli extended their simulation studies of particle deposition in turbulent boundary layer from spherical particles to elongated particles of different aspect ratio and density [2–4]. Thus, varying the particle response time and particle inertia. Rigid elongated particles were regarded as point particles. Collisions between particles were neglected, and collisions of particles with the wall was not fully resolved, i.e., only the wall-normal velocity of a particle was reversed upon impact. Creeping flow around the particle is assumed, and the calculation of hydrodynamic force and torque follows the analytical solution presented by Kim and Karrila [5]. Comparing non-spherical particles to spherical particles, they found that the wallward drift increased with the particle length, and thus the longest particles deposited near the wall at a higher rate.

Lindström, and later Andric extended fibre modelling from rigid fibres to flexible fibres [6,7]. In their approach they followed earlier work of Schmid et.al [8,9] who studied the flocculation behavior of flexible fibres in shear flow. Ca. 7 to 10 spheroids, i.e., rigid elements were linked together in the model for one flexible fibre. This, however, increased the simulation effort. Their model was capable to consider inertial effects and included particle-particle interaction. Back-coupling of forces from the particle exerted on the fluid was considered in the code, however not actively used in their simulation work. Findings of their study were that the specific viscosity for non-straight but curved fibres increased with the fibre curvature. In suspension flow, flexible fibres tended to align with the vorticity axis. This was in difference to rigid fibres which tended to align in the shear-plane [10].

Zhao and van Wachem extended their simulation studies and included effects of particle motion on the fluid motion [11]. Particles were coupled to the fluid by adding a source term which represented the sum of the drag force of particles in one fluid cell averaged over the volume of the fluid cell. They also considered particle-particle interaction and particle-wall interaction. Contact detection was performed by placing small spheres at the hull of one spheroid and thus using common contact detection algorithms for spherical particles. The repelling force was calculated using a Hertzian-like force model. Comparing their findings to findings of Marchioli and Soldati [4], they found that the turbulent kinetic energy decreased by 4.8% for suspensions of spheroids at a volume concentration of 0.0219%. Elongated particles were orientated randomly in the channel center. Closer to the wall particle orientation was preferen-

tially into the flow direction. They found the effect of the particle-wall interaction more pronounced, which was attributed to a more realistic interaction model.

Common in the above studies is that the authors used the same test geometry: a rectangular channel (dimension: 4π, 2, 2π, in x, y, z) which is wall bounded in the *y*-direction, and cyclic in the *x*-, and *z*- direction. The test case was based on studies of turbulent channel flow performed by Kim et.al. [12]. Following their settings, Marchioli and Soldati [3] used a semi-spectral method to solve the fluid motion. Lindström and Uesaka [6], Andric et.al. [13], as well as Zhao and van Wachem [11] used a finite-volume solver to simulate the Navier-Stokes equation.

Differently, the research group of Salcudean and Gartshore focused on simulation of fibre suspension flow in process equipment, i.e., the head-box of a paper machine, a hydrocyclone, and in a slotted channel [14–16]. To solve for the fluid motion, they used LES and RANS approaches, i.e., not resolving all flow structures. Elongated particles were modelled as stiff and flexible fibres. Flexible fibres were again modelled as chain of 4 spheroids linked together. A wall model was developed to account for fibre-wall interaction. Specifically, the wall was resolved by a fine mesh, smaller than the spheroid elements. Calculating the normal and tangential force, a force was applied on the spheroid element in contact with the wall being large enough to prevent the fibre from penetrating the wall. Hydrodynamic drag and torque interaction followed the work of Kim and Karilla [5] for creeping flow around the spheroid. Mass and lift forces were neglected. They found an accumulation of fibres in the vicinity of the wall. For a fibre-suspension in a wall bounded channel flow, they found an accumulation of fibres at a distance of the wall equal to their half-length.

2 MODELING APPROACH

We use an open-source CFD-DEM code to solve for the particle motion in a dilute fibre-suspension. The Navier-Stokes equations are solved using OpenFOAM (The OpenFOAM Foundation, 2014). Particles are placed into the developed flow field. Particle motion is solved with LIGGGHTS®. The coupling to the fluid is performed with CFDEM®coupling [17], which was extended to account for non-spherical, elongated stiff particles.

The translational and rotational motion of the fibre (in an inertial frame of reference) can be described by Newton's Equation of motion:

$$m_p \, d_t \mathbf{v} = \mathbf{f}^h + \mathbf{f}^w + \mathbf{f}^c \ , \tag{1}$$

$$\frac{d}{dt}\left(\mathbf{I}\cdot\boldsymbol{\omega}\right) = \mathbf{t}^h + \mathbf{t}^c \, . \tag{2}$$

Here, m_p is the mass of the prolate spheroid, and $\mathbf{I}$ is the moment of inertia tensor for a prolate spheroid. $\mathbf{f}^h$ and $\mathbf{t}^h$ are force and torque exerted on the particle by hydrodynamic interaction. $\mathbf{f}^c$ and $\mathbf{t}^c$ are interaction force and torque due to particle collision with the wall and/or other particles. $\mathbf{f}^w$ are body forces on the fibre. On the particle side (LIGGGHTS®), the elongated particle is represented as a spherocylinder, i.e., a cylinder with to half-spheres on each end of the cylinder (Figure 1a). The geometries are described by the cylinder length l and the cylinder diameter c. The radius of the half-sphere is thus $c/2$. It is possible to account for additional particle roughness, i.e., fibrils of a cellulose fibres. The height of the roughness is defined by δ_{rough} in our model.

For computing the fluid interaction forces and torques, the elongated particle is represented as a spheroid (Figure 1b). There is an analytical solution for spheroids under creeping flow conditions presented by Kim and Karrila [5], which we follow in the hydrodynamic interaction.

The major semi-axis *a* of the spheroid equals half the length of the cylinder, $a = l/2$. The minor semi-axis of the spheroid *b* is defined such that the hydrodynamic properties of the cylinder and the spheroid in shear-flow are identical. According to Cox [18], *b* calculates to:

$$b = \frac{1}{2.48} c \sqrt{\ln\left(\lambda_{cylinder}\right)} \quad . \tag{3}$$

$\lambda_{cylinder}$ is the aspect ratio of the spherocylinder, defined as $\lambda_{cylinder} = l/c$.

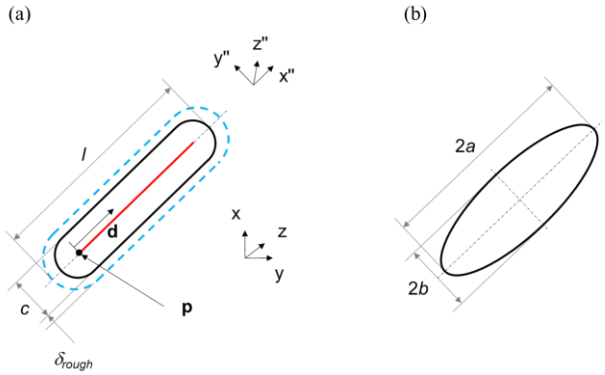

Figure 1: Schematic representation of the spherocylinder (a), and the prolate spheroid (b). *l* and *c* are the length and the diameter of the spherocylinder. **p** and **d** are the origin of the line segment and its (normalized) direction vector. δ_{rough} represents the particle surface roughness. *a*, and *b* are the major and minor semi-axis of the spheroid respectively. The global and particle associated Cartesian coordinate systems are indicated by (x,y,z) and (x",y",z") respectively.

Point-volume particles are assumed, and the fluid translational velocity **u**, as well as the local rotation rate **Ω**, are taken from the fluid cell coinciding with particle center, defined as $\mathbf{p} + \left(l - c\right)\mathbf{d}/2$.

2.1 Hydrodynamic Interactions

Our model for the hydrodynamic interaction coincides with the model presented by Lindström and Uesaka [6]. Assuming creeping flow, hydrodynamic force $\mathbf{f}^h$ and hydrodynamic torque $\mathbf{t}^h$ will be dominated by viscous effects modeled as:

$$\mathbf{f}^{v} = \mathbf{A}^{v} \cdot \left[\mathbf{u} - \mathbf{v}\right] \quad . \tag{4}$$

$$\mathbf{t}^{v} = \mathbf{C}^{v} \cdot \left[\mathbf{\Omega} - \boldsymbol{\omega}\right] + \mathbf{H}^{v} \cdot \dot{\boldsymbol{\gamma}} \, . \tag{5}$$

Here **v** is the fibre velocity at its center of mass position. $\dot{\boldsymbol{\gamma}}$ is the rate of strain tensor $\dot{\boldsymbol{\gamma}} = \left[\nabla\mathbf{u} + \left(\nabla\mathbf{u}\right)^{T}\right]/2$. $\mathbf{A}^{v}$, $\mathbf{C}^{v}$, and $\mathbf{H}^{v}$ are hydrodynamic resistance tensors defined as:

$$\mathbf{A}^{v} = 3\pi\eta l \left[Y^{A}\boldsymbol{\delta} + \left(X^{A} - Y^{A}\right)\mathbf{d}\otimes\mathbf{d}\right] \quad . \tag{6}$$

$$\mathbf{C}^{v} = \pi\eta l^{3}\left[Y^{C}\boldsymbol{\delta} + \left(X^{C} - Y^{C}\right)\mathbf{d}\otimes\mathbf{d}\right]. \tag{7}$$

$$\mathbf{H}^{v} = \pi\eta l^{3} Y^{H}\left(\boldsymbol{\varepsilon}\mathbf{d}\right)\otimes\mathbf{d} \, . \tag{8}$$

δ and **ε** denote the unit tensor and the permutation tensor. The parameters X^A, Y^A, X^C, Y^C, and Y^H depend on the eccentricity $e = \left(1 - b^2/a^2\right)^{1/2}$ of the prolate spheroid [6]. Previous work [6] also introduced a term considering inertial effects, i.e., an inertial drag force $\mathbf{f}^I$ and torque $\mathbf{t}^I$.

The resulting total hydrodynamic force $\mathbf{f}^h$ and hydrodynamic torque $\mathbf{t}^h$ on an elongated particle thus calculates to:

$$\mathbf{f}^h = \left(\mathbf{A}^v + \mathbf{A}^I\right)\cdot\left[\mathbf{u}-\mathbf{v}\right]. \tag{9}$$

$$\mathbf{t}^h = \left(\mathbf{C}^v + \mathbf{C}^I\right)\cdot\left[\mathbf{\Omega}-\boldsymbol{\omega}\right] + \left(\mathbf{H}^v + \mathbf{H}^I\right)\cdot\dot{\boldsymbol{\gamma}}. \tag{10}$$

As described by Fan and Ahmadi [19], the equations for the particle motion (eqn. 1, and eqn. 2) are of stiff nature, and need to be solved using a forward-differencing scheme. To do so, the fluid-particle interactions terms in the governing equations must be decomposed into and an explicit (indicated by subscript '*exp*' below) and an implicit contribution. Furthermore, it is useful to solve the translational equation of motion in the inertial reference frame, and that for rotational motion in a reference frame aligned with the principal axes of the particles. The latter is indicated by primed variables in what follows. In our work we also consider a simple model for added mass effects (due to liquid rotating with the particles). In analogy to Fan and Ahmadi [19], the equations of motion read:

$$\left(1+C_{addM}\,\rho_f/\rho_p\right)m_p d_t\mathbf{v} = \mathbf{f}_{\exp} + \mathbf{K}_{sl}\cdot\left(\mathbf{u}-\mathbf{v}\right), \tag{11}$$

$$\mathbf{I}_p^{'}\cdot d_{t^{'}}\left(\boldsymbol{\omega}^{'}\right) + \boldsymbol{\omega}^{'}\times\left(\mathbf{I}_p^{'}\cdot\boldsymbol{\omega}^{'}\right) = \mathbf{t}_{\exp}^{'} + \mathbf{K}_{sl,rot}^{'}\cdot\left(\mathbf{\Omega}^{'}-\boldsymbol{\omega}^{'}\right), \text{ with} \tag{12}$$

$$\mathbf{I}_p^{'} = \mathbf{I}^{'}\left(1+C_{add}\,\rho_f/\rho_p\right) \tag{13}$$

Here $\mathbf{K}_{sl}$ and $\mathbf{K}_{sl,rot}$ are the diagonal part of the translational and rotational drag resistance tensors defined above, respectively. Note that $\mathbf{I}$' is the moment of inertia tensor in the body-fixed coordinate system, which is constant for each particle.

We now apply a Crank-Nicholson forward discretization scheme (with CN_α being the Crank-Nicholson blending factor) to arrive at the following explicit evolution equations for the translational and rotation speed of each particle at timestep n+1:

$$\mathbf{v}^{\{n+1\}} = \frac{\mathbf{v}^{\{n\}} + \dfrac{\Delta t}{\left(1+C_{addM}\,\rho_f/\rho_p\right)m_p}\left[\mathbf{f}_{\exp}^{\{n\}} + \mathbf{K}_{sl}^{\{n\}}\cdot\left(\mathbf{u}^{\{n\}} - \left(1-CN_\alpha\right)\mathbf{v}^{\{n\}}\right)\right]}{1+\Delta t\,\mathbf{K}_{sl}^{\{n\}}\,CN_\alpha/\left[\left(1+C_{addM}\,\rho_f/\rho_p\right)m_p\right]}, \tag{14}$$

$$\boldsymbol{\omega}_i^{'\{n+1\}} = \frac{\boldsymbol{\omega}_i^{'\{n\}} + \dfrac{\Delta t}{\mathbf{I}_{p,ii}^{'}}\left(\mathbf{t}_{tot,i}^{'\{n\}} - \left[\boldsymbol{\omega}_i^{'\{n\}}\times\left(\mathbf{I}_p^{'}\cdot\boldsymbol{\omega}_i^{'\{n\}}\right)\right]_i + \mathbf{K}_{sl,rot,i}^{'\{n\}}\,CN_\alpha\,\boldsymbol{\omega}_i^{'\{n\}}\right)}{1+\Delta t\,\mathbf{K}_{sl,rot,i}^{'\{n\}}\,CN_\alpha/\mathbf{I}_{p,ii}^{'}}, \text{ with} \tag{15}$$

$$\mathbf{t}_{tot}^{'\{n\}} = \mathbf{t}_{\exp}^{'\{n\}} + \mathbf{K}_{sl,rot}^{'\{n\}}\cdot\left(\mathbf{\Omega}^{'\{n\}} - \boldsymbol{\omega}^{'\{n\}}\right) \tag{16}$$

We have verified our implementation against the analytical solution of Jeffery [20]. Thus, an elongated particle (of zero mass) in a linear shear flow will rotate with a time period:

$$\tau = \frac{2\pi}{\dot{\gamma}_p} = \frac{2\pi\left(\lambda+1/\lambda\right)}{\dot{\gamma}}. \tag{17}$$

$\dot{\gamma}_p$ is the flipping frequency of the particle, and $\dot{\gamma}$ is the fluid shear rate. λ is the aspect ratio of the spheroid defined as, $\lambda = a/b$. A characteristic of the rotation of elongated particle in laminar shear flow is, that the particles remain in their initial orbit of rotation, i.e., the initial

orientation of the particle rotational axis with respect to the shear plane remains constant [5,21]. The orbit constant C is defined as

$$C = \lambda \tan(\theta)\left(\lambda^2 \sin^2(\phi) + \cos^2(\phi)\right)^{1/2}, \text{with} \tag{18}$$

$$\tan(\phi) = \lambda \tan\left(\frac{\dot{\gamma} t}{\lambda + 1/\lambda}\right), \tag{19}$$

$$\tan(\theta) = \frac{C\lambda}{\left(\sin^2(\phi) + \lambda^2 \cos^2(\phi)\right)^{1/2}}. \tag{20}$$

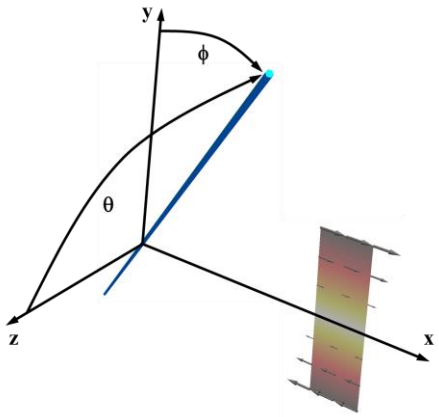

Figure 2: Coordinate system and definition of the Cartesian and polar coordinates with respect to the shear plane.

Figure 3a, compares the orientation angle ϕ from our simulation of an elongated particle, $\lambda = 10$, in a linear shear flow, $\dot{\gamma} = 666 s^{-1}$, to the analytical solution derived by Jeffery. The initial orientation is: $\phi = \pi/2$, and $\theta = \pi/2$, yielding an orbit constant of $C = 0.709$. In Figure 3b we plot the angular velocity, and observe that the simulation results perfectly represent the analytical solution for low density ratios. However, for increased particle density and thus increased particle inertia, Lundell and Carlson [22] found that the time-dependent flipping behavior of the elongated particle changes to a time independent rotational motion of the elongated particle. Figure 3c and d show the angular position and the angular velocity of a particle, initially orientated in shear plane ($C = \infty$) with a density ratio (particle to fluid) of 5000, respectively. We find, that the oscillation frequency increases and the particle actually is never at rest, i.e. $\omega > 0$. Thus, our code captures very well the transition from a time-dependent flipping to a time-independent rotational motion.

We note in passing that Rosén et.al. [21,23] performed detailed simulations of a single elongated particle, fully resolving the fluid-particle forces. He showed that at increased fluid inertia, elongated particles leave their initial orbit and drift towards a stable orbit. Unfortunately, our code is currently not able to account for this effect. Thus, simulations performed are yet limited to cases of small particle Reynolds number where we can assume creeping flow around the particle.

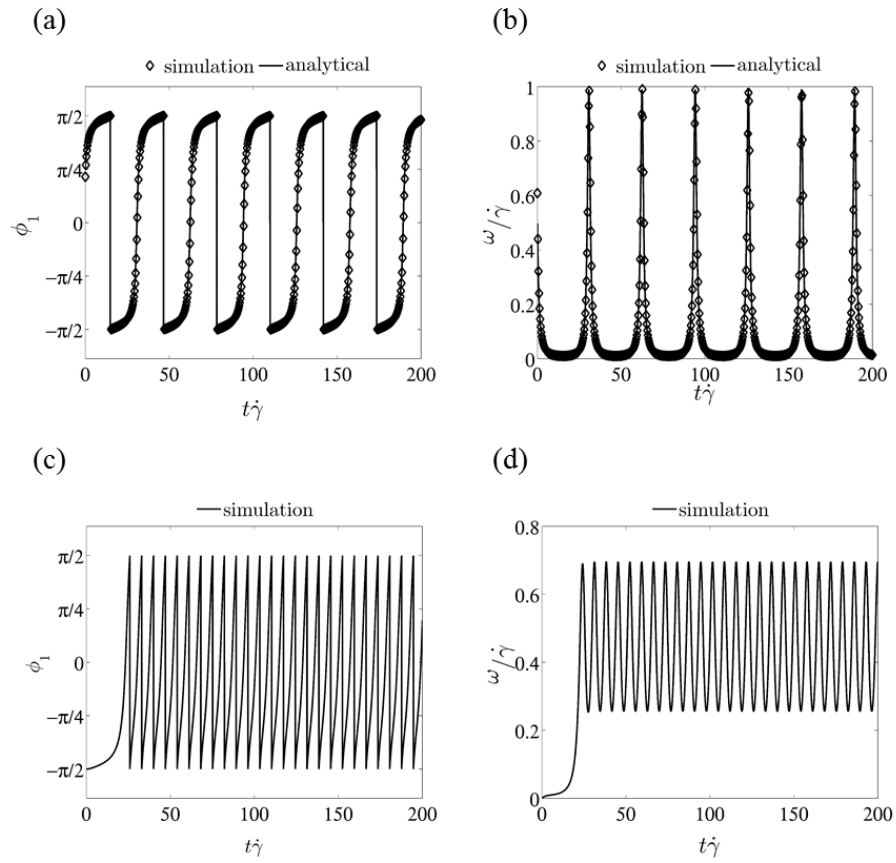

Figure 3: Time dependent orientation angle ϕ, and angular velocity ω, for an elongated particle, $\lambda = 10$, in linear shear flow. The particle relative density is 0.001 (panel a and b), and 5000 (panel c and d).

2.2 Contact Force and Torque

Calculation of contact force $\mathbf{f}^c$ and contact torque $\mathbf{t}^c$ follows a linear spring-dashpot model in normal and tangential direction [24,25]:

$$\mathbf{f}_p{}^c = \left(k_n \delta \mathbf{n}_{ij} - \gamma_n \mathbf{v}\mathbf{n}_{ij}\right) + \left(k_t \delta \mathbf{t}_{ij} - \gamma_t \mathbf{v}\mathbf{t}_{ij}\right) \ . \tag{21}$$

k_n and k_t are the normal and tangential spring stiffness, and γ_n and γ_t are the normal and tangential damping coefficient respectively. The vector $\mathbf{n}_{ij}$ and $\mathbf{t}_{ij}$ are the normal and tangential directions of the collision. Within the surface roughness region, the roughness adds to the total collision force, $\mathbf{f}^c = \mathbf{f}_p{}^c + \mathbf{f}_{rough}{}^c$. The formulation of $\mathbf{f}_{rough}{}^c$ is identical to the collision force of the particle. The torque is calculated as the cross product of the contact force $\mathbf{f}^c$ and the distance between the bodies $\mathbf{r}$.

$$\mathbf{t}^c = \mathbf{f}^c \times \mathbf{r} \ . \tag{22}$$

The contact detection algorithm follows the calculation of a line intersecting with another line (particle-particle), or a triangle (particle-wall, see Figure 4 for an illustration). The implementation follows the strategy proposed by Schneider and Eberly [26], and below the main idea of the algorithm is summarized. More details can be found in König [27].

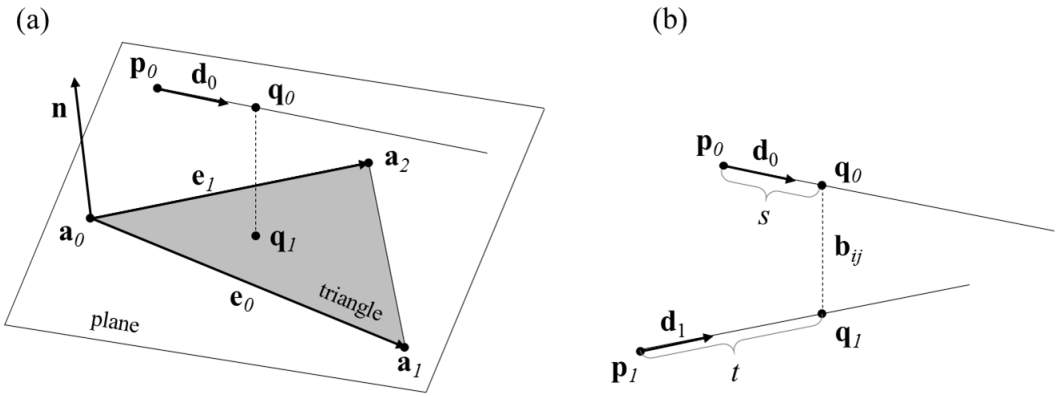

Figure 4: Graphical illustration of the (a) line-triangle interaction, and (b) line-line interaction [26,27].

The line segment is presented by its point of origin, the direction of orientation and its extension: $\mathbf{l}_0(s) = \mathbf{p}_0 + s\mathbf{d}_0$, and $\mathbf{l}_1(t) = \mathbf{p}_1 + t\mathbf{d}_1$. The two points on the line segment with the smallest distance are $\mathbf{q}_0$ and $\mathbf{q}_1$. The length of the vector $\mathbf{d}_{ij}$ presents the distance between both lines. The triangle segment is presented by $\mathbf{a}(u,v) = \mathbf{a}_0 + u\mathbf{e}_0 + v\mathbf{e}_1$ with $\mathbf{e}_0 = \mathbf{a}_1 - \mathbf{a}_0$, and $\mathbf{e}_1 = \mathbf{a}_2 - \mathbf{a}_0$. All points within the triangle are represented by $0 \le u$, $v \le 1$, subject to the constraint $u + v \le 1$. The code first checks if the elements, lines or line-triangle, are parallel to each other by calculating the dot product, $\mathbf{d}_0 \cdot \mathbf{n}$ and $\mathbf{d}_0 \cdot \mathbf{d}_1$, where $\mathbf{n}$ is the normal vector of the plane, $\mathbf{n} = \mathbf{e}_0 \times \mathbf{e}_1$. If the result is 0, both elements are parallel to each other. The minimum distance between the elements is found by minimizing the square distance function. In case the closest point of the two elements is of smaller distance than $c/2$ for line-triangle, or c for line-line interaction, the two elements are in contact with each other. In case the contact point is found on either end of the line segment, contact detection for spherical particles is applied.

While particle-particle interactions have been verified by König [27], selected results of the particle-wall interaction verification study are presented below. Specifically, the rebound translational v_x^+ and rotational ω_z^+ velocities were calculated following Kodam et.al. [28]:

$$\omega_z^+ = \frac{m \cdot v_x^- (1+\varepsilon) h' \cos(\alpha' + \theta)}{I_{zz} + m h'^2 \cos^2(\alpha' + \theta)} \tag{23}$$

$$v_x^+ = \omega_y^+ h' \cos(\alpha' + \theta) - \varepsilon v_x^- \tag{24}$$

Here the superscript + and – denote the post impact and pre impact quantities. v and ω are components of the translational and rotational velocity of the cylinder. ε is the coefficient of restitution, m is the mass of the prolate spheroid and I_{zz} is the spheroid inertia around the shorter semi-axis. h' and angle α' are geometrical values of the cylinder (Figure 5a). To apply the analytical solution, a rectangular cylinder corresponding to the spherocylinder had to be projected into the spherocylinder. Figure 5a illustrates the spherocylinder and its corresponding rectangular cylinder for a certain inclination θ. The shape of the projected cylinder (i.e., α', h', l', and c') changes with θ as follows:

$$c' = c \sin(\theta) \ . \tag{25}$$

$$l' = l - c(1 - \sin(\theta)) . \tag{26}$$

$$h' = \sqrt{c'^2 + l'^2}\,/\,2\,. \tag{27}$$

$$\alpha' = \arctan\left(c'/l'\right)\,. \tag{28}$$

Figure 5b compares the simulation results to the analytical solution, showing excellent agreement.

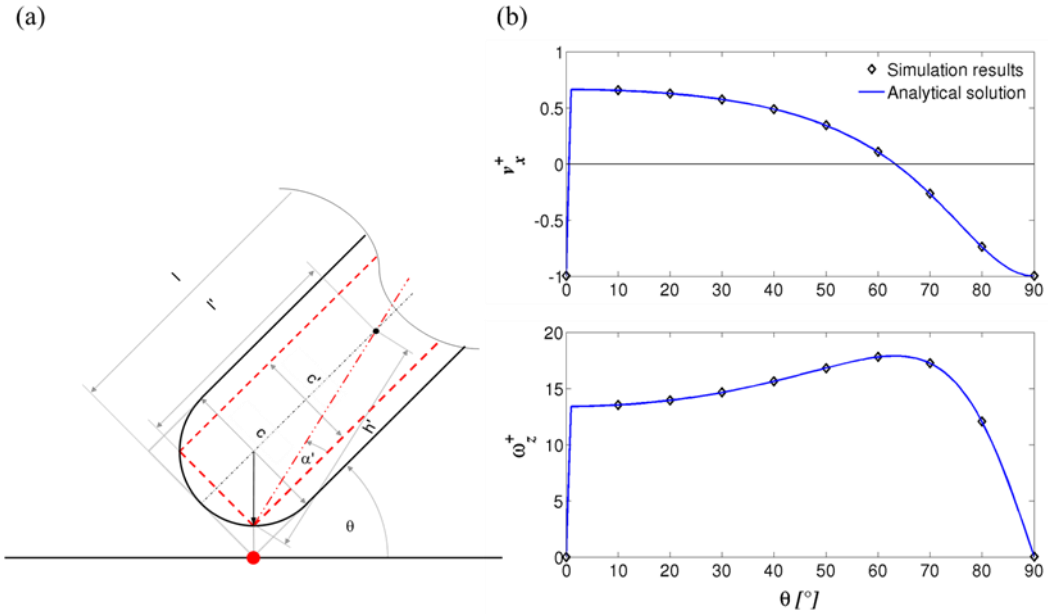

Figure 5: a: Fibre-wall impact presenting the sphero-cylinder and its corresponding rectangular cylinder. b: Comparison of simulation results to an analytical solution for rectangular cylinders [28]. Translational v_x^+ and rotational ω_z^+ velocity for different inclination angles θ.

3 RESULTS

In this section we illustrate our methodology by considering a general suspension flow test case, i.e., flow in a torus as previously considered by Redlinger-Pohn et al. [29]. The fibre-fluid density ratio is 1.3. The aspect ratio of the fibres was varied to model differently-sized fibres. The flow field was solved with OpenFOAM®, version 2.3.0. Time derivatives were approximated with a second-order Euler backwards scheme, and convective terms were approximated with the second-order Gauss linear interpolation scheme. The PISO algorithm was used to solve the equations. Settings for the fluid solver were in accordance with settings used by Andric et.al. [7].

3.1 The Motion of a Fibre Suspension in a Torus

Due to the curvature of coiled tubes the resulting flow field differs from the flow field in a straight pipe flow. In order to approximate such tubes, we here consider flow in a closed torus as an academic test case [30]. It is well known that centrifugal forces lead to a deflection of the fluid flow towards the outer bent, thus yielding a pressure gradient in the cross section [31,32]. Consequently, a secondary flow arises within the cross section from the outer bent *O* towards the inner bent *I* along the pipe wall, and from the inner bent to the outer bent along the equatorial mid plane. This secondary motion u_{sec} is called Dean flow, and the intensity is quantified by the Dean number *Da*:

$$\kappa = d/D\,. \tag{29}$$

$$u_{\text{sec}} = u_{bulk}\sqrt{\kappa}\ . \tag{30}$$

$$Re = \frac{u_{bulk}\cdot d}{\nu}\ . \tag{31}$$

$$Da = \frac{u_{\text{sec}}\cdot d}{\nu} = \text{Re}\cdot\sqrt{\kappa}\ \ . \tag{32}$$

The torus is sketched in Figure 6. d and D are the diameter of the tube cross section and the coil diameter of the torus respectively. u_{bulk} is the mean bulk velocity of the fluid, and ν is the kinematic viscosity of the fluid. The section above the equatorial mid-line is defined as upper half (*UH)*, and the section below is defined as lower half (*LH)*. *I* and *O* denote the inner and outer wall of the torus. Cartesian coordinates are donated as (x,y,z), and the corresponding toroidal coordinates as (r,φ,Θ).

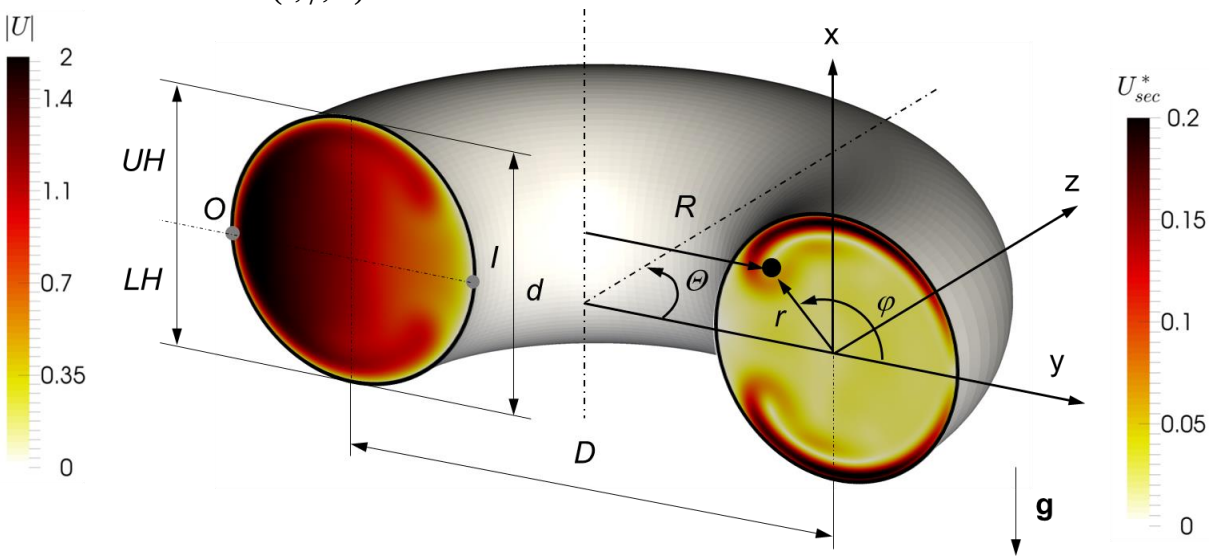

Figure 6: Schematic representation of the half torus in the Cartesian (x,y,z) and toroidal (r,φ,Θ) coordinate system. **g** denotes the direction of gravity. *D* and *d* present the torus and pipe diameter. *I* and *O* denote the inner and outer wall of the torus. Projected in the cross section is a typical flow profile of a laminar toroidal flow. Left cross section: flow in the stream wise direction, right cross section: secondary motion (*Da* = 1049, figure adapted from [29]).

Simulation of the toroidal flow is documented in Redlinger-Pohn et.al. [29]. The position of the Dean vortex is indicated by a black dot in Figure 6. At this position the secondary motion describes a rapid change in the flow direction.

Particles introduced into the flow field will be affected by the secondary motion. Depending on their mass and density, and thus their terminal settling velocity u_{set} particles will be (i) mixed in the cross section [33] or (ii) settle towards the *LH* and are pushed to the inner bent *I* by the secondary motion [34]. At the latter position we find particles in a region of low stream-wise fluid velocity.

In an extensive numerical study, fibres of different aspect ratio (ranging from 2 to 160) were introduced into the above shown flow profiles [29]. Here we document some additional findings from our previous simulation results that are illustrated in Figure 7: colored in yellow are regions where the (vertical) secondary motion exceeds the terminal settling velocity, and thus particles are lifted against gravity. Regions where the fibre settles in direction of the gravity are indicated in blue. We find, that regions in the *UH* where longer (and thus heavier)

fibres (λ = 160) are lifted are confined to the inner wall of the torus. Specifically, these regions are located at the outer bent where the secondary motion is strongest, and extend to the center of the Dean vortex. Regions where the smaller fibres (λ = 2) experience a lift are significantly larger, explaining the more homogeneous distribution of these fibres.

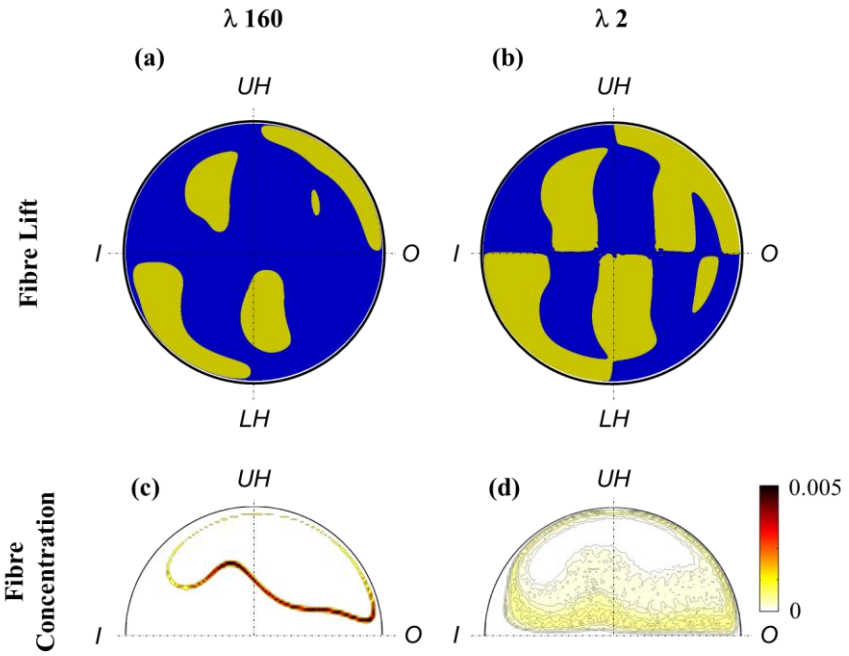

Figure 7: a and b: Sum of the secondary motion in direction of gravity and the fibres' terminal settling velocity. Yellow: secondary motion exceeding the settling velocity. c and d: Relative fibre concentration. *Da* = 1049 for this simulations.

The consequence of the fact that longer fibres only experience lift in certain regions explains the accumulation into a narrow band. Here the longer fibres orbit in the cross section in the *UH* (Figure 7c). Especially close to the equatorial midplane, where the fibres slowly move from the inner bent *I* to the outer bent *O*, we find a high concentration of fibres. Most likely, fibres will entangle in these regions and form a larger fibre-flock. Smaller fibres are more effectively mixed by the secondary motion, and are distributed more homogenously in the torus' cross section (see Figure 7d). The consequence is a fibre length-dependent segregation in flow direction, with the longer fibres moving (on average) faster than the fluid.

4 CONCLUSION AND OUTLOOK

We present details of an open-source code for the simulation of non-spherical, elongated particles suspended in a fluid. In our modeling approach we follow a strategy involving (i) rigid elongated particles, (ii) one-way coupling to the fluid, as well as (iii) fibre-fibre and fibre-wall interactions. For the particle interaction we represent the particle as spherocylinders, and detect the point of contact by a line-segment algorithm. Thus, we do not represent the particle surface by multiple spheres, allowing a comparably rapid calculation of the contact point. The code is successfully validated against standard cases for elongated particles, e.g., the Jeffery orbit.

Finally, we performed a simulation study of a fibre suspension in a torus. A fibre length-depended segregation was observed. The reason for this phenomena is that fibres are lifted by

the secondary motion in the upper half of the torus, i.e., they can move against gravity. This lifting effect differs for fibres of variable length. As a consequence we observe a localized high concentration of long fibres in the torus' cross section, while smaller fibres are rather homogeneously distributed. This segregation is certainly of key importance for the transport rate of fibres through the torus.

Future studies may include the simulation of fibre suspensions at higher Reynolds numbers, i.e., that exceeding the laminar flow regime. The investigation of more test cases used in literature (e.g., by Marchioli and Soldati [4], or Andric et.al. [7]) may pave the way towards an industrial application of our simulation tool. However, a more realistic flexible fibre model (than presented in our present work) should be used for these cases. This is because the formation of fibre aggregates certainly becomes a dominating effect at fibre concentrations relevant for industrial applications. Unfortunately, flexible fibre models require significantly more computational resources compared to the rigid fibre model in the present contribution.

5 ACKNOWLEDGEMENT

JDRP, LMK, and SR acknowledge partial support from FLIPPR (http://www.flippr.at/), as well from NAWI Graz by providing access to dcluster.tugraz.at. CK and CG acknowledge funding through the NanoSim project (http://www.sintef.no/projectweb/nanosim).

6 REFERENCES

[1] H.I. Andersson, A. Soldati, Anisotropic particles in turbulence: Status and outlook, Acta Mech. 224 (2013) 2219–2223. doi:10.1007/s00707-013-0926-y.

[2] C. Marchioli, A. Soldati, Rotation statistics of fibers in wall shear turbulence, Acta Mech. 224 (2013) 2311–2329. doi:10.1007/s00707-013-0933-z.

[3] C. Marchioli, M. Fantoni, A. Soldati, Orientation, distribution, and deposition of elongated, inertial fibers in turbulent channel flow, Phys. Fluids. 22 (2010) 1–14. doi:10.1063/1.3328874.

[4] A. Soldati, C. Marchioli, Physics and modelling of turbulent particle deposition and entrainment: Review of a systematic study, Int. J. Multiph. Flow. 35 (2009) 827–839. doi:10.1016/j.ijmultiphaseflow.2009.02.016.

[5] S. Kim, S.J. Karrila, Microhydrodynamics: Principles and Selected Applications, Dover Publications, 2005. https://books.google.at/books?id=_8llnUUGo0wC.

[6] S.B. Lindström, T. Uesaka, Simulation of the motion of flexible fibers in viscous fluid flow, Phys. Fluids. 19 (2007). doi:10.1063/1.2778937.

[7] J. Andrić, S.T. Fredriksson, S.B. Lindström, S. Sasic, H. Nilsson, A study of a flexible fiber model and its behavior in DNS of turbulent channel flow, Acta Mech. 224 (2013) 2359–2374. doi:10.1007/s00707-013-0918-y.

[8] C.F. Schmid, D.J. Klingenberg, Mechanical Flocculation in Flowing Fiber Suspensions, Phys. Rev. Lett. 84 (2000) 290–293. doi:10.1103/PhysRevLett.84.290.

[9] C.F. Schmid, L.H. Switzer, D.J. Klingenberg, Simulations of fiber flocculation: Effects of fiber properties and interfiber friction, J. Rheol. (N. Y. N. Y). 44 (2000) 781. doi:10.1122/1.551116.

[10] L. Jianzhong, Z. Weifeng, Y. Zhaosheng, Numerical research on the orientation distribution of fibers immersed in laminar and turbulent pipe flows, J. Aerosol Sci. 35 (2004) 63–82. doi:10.1016/S0021-8502(03)00388-4.

[11] F. Zhao, B.G.M. Van Wachem, Direct numerical simulation of ellipsoidal particles in turbulent channel flow, Acta Mech. 224 (2013) 2331–2358. doi:10.1007/s00707-013-0921-3.

[12] J. Kim, P. Moin, R. Moser, Turbulence statistics in fully developed channel flow at low Reynolds number, J. Fluid Mech. 177 (1987) 133. doi:10.1017/S0022112087000892.
[13] J. Andrić, S.B. Lindström, S. Sasic, H. Nilsson, Rheological properties of dilute suspensions of rigid and flexible fibers, J. Nonnewton. Fluid Mech. 212 (2014) 36–46. doi:10.1016/j.jnnfm.2014.08.002.
[14] Z. Wang, Numerical Simulation of Fiber Separation in Hydrocyclones, Master Thesis, The University of British Columbia, 2002.
[15] X. Zhang, Fiber Orientation in a Headbox, Master Thesis, The University of British Columbia, 2001.
[16] S. Dong, Modeling of Fiber Motion in Pulp and Paper Equipment, PhD Thesis, The University of British Columbia, 2002.
[17] C. Goniva, C. Kloss, N.G. Deen, J.A.M. Kuipers, S. Pirker, Influence of rolling friction on single spout fluidized bed simulation, Particuology. 10 (2012) 582–591. doi:10.1016/j.partic.2012.05.002.
[18] R.G. Cox, The motion of long slender bodies in a viscous fluid Part 1. General theory, J. Fluid Mech. 44 (1970) 791. doi:10.1017/S002211207000215X.
[19] F.-G. Fan, G. Ahmadi, A sublayer model for wall deposition of ellipsoidal particles in turbulent streams, J. Aerosol Sci. 26 (1995) 813–840. doi:10.1016/0021-8502(95)00021-4.
[20] G.B. Jeffery, The Motion of Ellipsoidal Particles Immersed in a Viscous Fluid, Proc. R. Soc. A Math. Phys. Eng. Sci. 102 (1922) 161–179. doi:10.1098/rspa.1922.0078.
[21] T. Rosén, M. Do-Quang, C.K. Aidun, F. Lundell, The dynamical states of a prolate spheroidal particle suspended in shear flow as a consequence of particle and fluid inertia, J. Fluid Mech. 771 (2015) 115–158. doi:10.1017/jfm.2015.127.
[22] F. Lundell, A. Carlsson, Heavy ellipsoids in creeping shear flow: Transitions of the particle rotation rate and orbit shape, Phys. Rev. E. 81 (2010) 016323. doi:10.1103/PhysRevE.81.016323.
[23] T. Rosén, F. Lundell, C.K. Aidun, Effect of fluid inertia on the dynamics and scaling of neutrally buoyant particles in shear flow, J. Fluid Mech. 738 (2014) 563–590. doi:10.1017/jfm.2013.599.
[24] P.A. Cundall, O.D.L. Strack, A discrete numerical model for granular assemblies, Géotechnique. 29 (1979) 47–65. doi:10.1680/geot.1979.29.1.47.
[25] S. Luding, Introduction to discrete element methods. Basic of contact force models and how to perform the micro-macro transition to continuum theory, Rev. Eur. Génie Civ. 12 (2008) 785–826. doi:10.3166/ejece.12.785-826.
[26] P.J. Schneider, D.H. Eberly, Geometric Tools for Computer Graphics, Elsevier, 2003. doi:10.1016/B978-1-55860-594-7.50023-0.
[27] L.M. König, Particle Separation in a Virtual Microfluidic Channel, Master Thesis, Graz University of Technology, 2015.
[28] M. Kodam, R. Bharadwaj, J. Curtis, B. Hancock, C. Wassgren, Cylindrical object contact detection for use in discrete element method simulations, Part II-Experimental validation, Chem. Eng. Sci. 65 (2010) 5863–5871. doi:10.1016/j.ces.2010.08.007.
[29] J.D. Redlinger-Pohn, L.A. Jagiello, W. Bauer, S. Radl, Mechanisitc Understanding of Size-Based Fibre Separation in Coiled Tubes, Int. J. Multiph. Flow. submitted (2016).
[30] T.J. Hüttl, R. Friedrich, Influence of curvature and torsion on turbulent flow in helically coiled pipes, Int. J. Heat Fluid Flow. 21 (2000) 345–353. doi:10.1016/S0142-727X(00)00019-9.
[31] W.R. Dean, XVI. Note on the motion of fluid in a curved pipe, London, Edinburgh, Dublin Philos. Mag. J. Sci. 4 (1927) 208–223. doi:10.1080/14786440708564324.

[32] I. Di Piazza, M. Ciofalo, Transition to turbulence in toroidal pipes, J. Fluid Mech. 687 (2011) 72–117. doi:10.1017/jfm.2011.321.
[33] T.K. Palazoglu, K.P. Sandeep, Effect of tube curvature ratio on the residence time distribution of multiple particles in helical tubes, LWT - Food Sci. Technol. 37 (2004) 387–393. doi:10.1016/S0023-6438(03)00013-6.
[34] P. Tiwari, S.P. Antal, M.Z. Podowski, Three-dimensional fluid mechanics of particulate two-phase flows in U-bend and helical conduits, Phys. Fluids. 18 (2006) 043304. doi:10.1063/1.2189212.